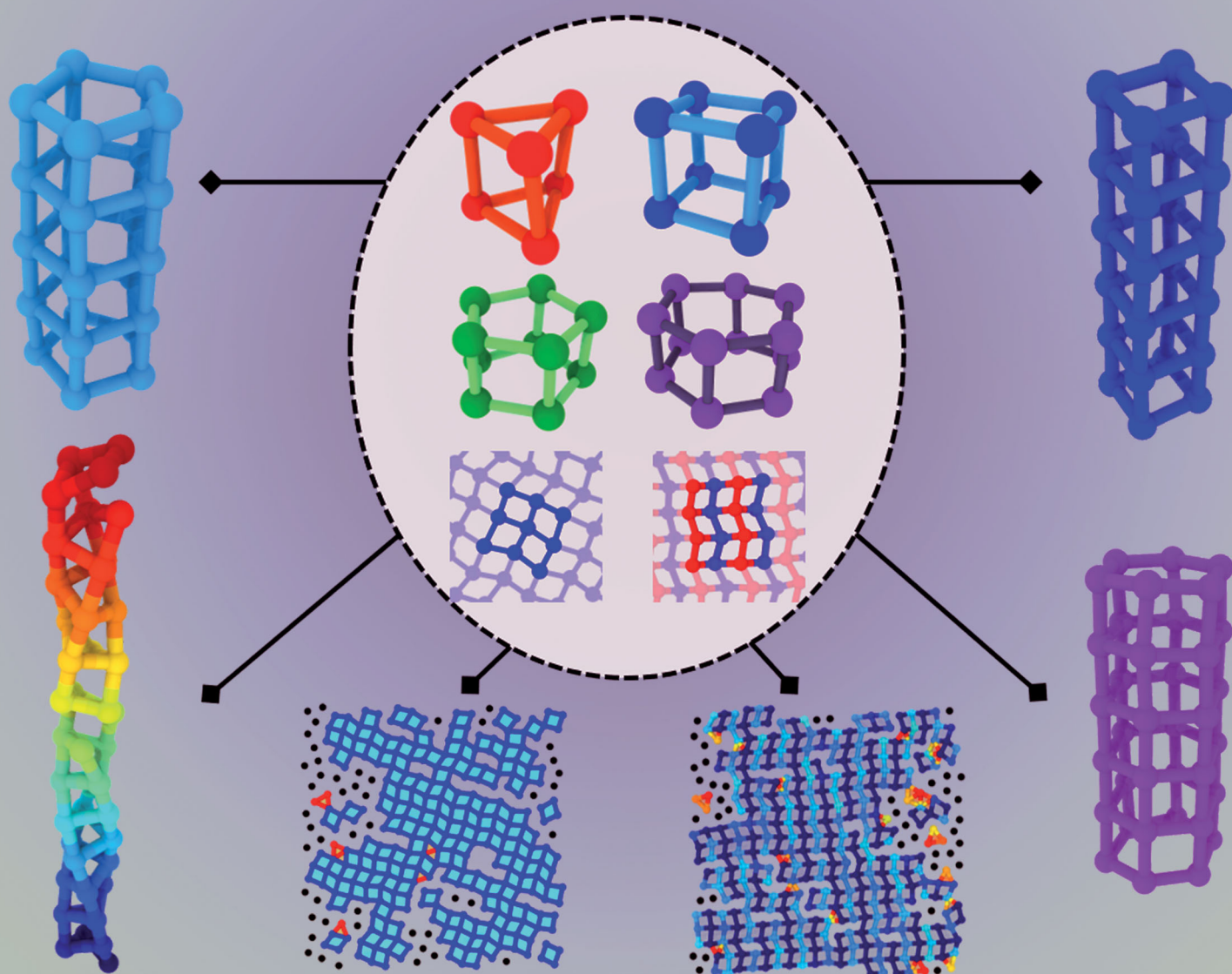


# PCCP

Physical Chemistry Chemical Physics

rsc.li/pccp



ISSN 1463-9076

**PAPER**

Amrita Goswami and Jayant K. Singh  
A general topological network criterion for exploring the  
structure of icy nanoribbons and monolayers



Cite this: *Phys. Chem. Chem. Phys.*, 2020, 22, 3800

# A general topological network criterion for exploring the structure of icy nanoribbons and monolayers†

Amrita Goswami <sup>a</sup> and Jayant K. Singh <sup>\*b</sup>

We develop intuitive metrics for quantifying complex nucleating systems under confinement. These are shown to arise naturally from the analysis of the topological ring network, and are amenable for use as order parameters for such systems. Drawing inspiration from qualitative visual inspection, we introduce a general topological criterion for elucidating the ordered structures of confined water, using a graph theoretic approach. Our criterion is based on primitive rings, and reinterprets the hydrogen-bond network in terms of these primitives. This approach has no *a priori* assumptions, except the hydrogen bond definition, and may be used as an exploratory tool for the automated discovery of new ordered phases. We demonstrate the versatility of our criterion by applying it to analyse well-known monolayer ices. Our methodology is then extended to identify the building blocks of one-dimensional *n*-sided prismatic nanoribbon ices.

Received 4th September 2019,  
Accepted 17th November 2019

DOI: 10.1039/c9cp04902a

rsc.li/pccp

## 1 Introduction

Confinement is known to cause deviations from bulk system properties,<sup>1–4</sup> imparting unique complexities to the structure determination of icy confined water. The structure and phase behaviour of quintessential confined systems, like that of two-dimensional monolayers and one-dimensional nanoribbons, are of enormous theoretical<sup>4–6</sup> and experimental interest.<sup>7,8</sup> However, well-defined simulation methodologies and methods of analysis for bulk systems like the mean squared displacement (MSD), often used as a broad indicator of phase transitions, may be unreliable for constrained ice systems. The reasons are two-fold: confined water often exhibits continuous freezing transitions,<sup>9–11</sup> and the mobility of water layers close to the confining sheet is lower than that of intermediate layers.<sup>12,13</sup> Parameters engineered to characterize phase transitions in simpler Lennard-Jones systems, inspired by the MSD, are not universally valid. For example, the Lindemann parameter, which has been used for melting studies,<sup>14,15</sup> fails for confined systems with attractive pores due to instabilities in the MSD.<sup>16</sup> Structure determination techniques, which are accurate for bulk water, are often intractable for nucleating water systems under confinement, as the hydrogen-bonding network (HBN) is

significantly influenced by the confining wall. Compared to bulk water, water under nanoscale confinement shows considerable polymorphic diversity.<sup>17</sup>

Visual inspection of the HBN, paired with the angle distribution, has been used in the literature for the analysis of confined water systems. Such techniques are often used for qualitative analyses<sup>5,10,11,18,19</sup> but are unable to describe the structures quantitatively. Voronoi tessellation<sup>20</sup> has been previously used to quantify the structures of two-dimensional confined ice systems. The bond orientational parameter has also been used for distinguishing the degree of square and hexagonal order in ice.<sup>21</sup> However, the bond orientational parameter has implicit *a priori* assumptions of the ice structures formed, and cannot be used as an exploratory tool. Moreover, none of these parameters has been successfully applied to one-dimensional nanoribbon ices, although axial and angular order parameters for distinguishing between square and pentagonal ice nanotubes have been used.<sup>1</sup> There is no single straightforward classification technique for confined ordered ice-like water that minimizes human involvement and assumptions, and emphasizes automated, reproducible, quantifiable structural elucidation.

Determining the connectivity of an ordered phase by using the primitive rings formed is a well-established technique of identification.<sup>22–27</sup> Ic (cubic ice) and Ih (hexagonal ice) are ice phases which are similar enough that their structural differences are not trivially discernible by casual inspection. A robust and intuitive classification of the building-blocks of Ic and Ih, based on primitive ring connectivity, has been formulated<sup>28</sup>

<sup>a</sup> Department of Chemical Engineering, Indian Institute of Technology Kanpur, Uttar Pradesh, 208016, India. E-mail: amritag@iitk.ac.in

<sup>b</sup> Department of Chemical Engineering, Indian Institute of Technology Kanpur, Uttar Pradesh, 208016, India. E-mail: jayantks@iitk.ac.in; Tel: +91-512-2596141

† Electronic supplementary information (ESI) available. See DOI: 10.1039/c9cp04902a

and used for homogenous and heterogenous bulk nucleation.<sup>29–31</sup> However, these topological network connectivity analyses, like other popular analyses including spherical harmonics based methods, suffer from a common shortcoming. All such classification techniques use a fixed-distance cutoff, after which further reductions or criteria are applied. These techniques work on the assumption that distance-based information is nearly equivalent to the HBN information. This implicit assumption is known to be valid for bulk systems of deeply supercooled water.<sup>32</sup> Thus, for such systems, the distance-based cutoff, corresponding to the first nearest-neighbor shell of the oxygen atoms (first minimum of the O–O radial distribution function) is a close approximation of the HBN, with negligible overcounting.<sup>28</sup>

The scenario is more complex for confined systems. Confined systems show a variety of ordered phases at temperatures much higher than the freezing point of the bulk liquid. Experimental results have predicted substantial temperature elevations of the freezing transition for water constrained within isolated carbon nanotubes, compared to the bulk phase.<sup>8</sup> Simulations have also shown that certain confined systems exhibit a freezing point as high as 390 K.<sup>33</sup> In particular, at high pressures or under strong confinement, we show that a fixed distance-cutoff creates connections between molecules which are not actually part of the HBN. Naive application of a topological network criterion based on a fixed distance cutoff, thus, necessarily fails by creating extraneous connections.

We summarize the main practical challenges of confined ice structure determination as follows:

1. Confined water has a high number of possible polymorphs of quasi-one and two-dimensional ice. These manifest even at elevated temperatures compared to the bulk. The ordered structures are highly sensitive to the geometry of the confining surface and hydrophobicity.

2. A molecule in confined water may not actually form a hydrogen-bond with every one of its nearest neighbours. This is because molecules forced within the first nearest-neighbour shell under the effect of confinement or high pressure may not fulfil the additional strict criterion of hydrogen bond formation. We show that not accounting for the hydrogen bonds can cause significant mis-identification of ice.

In the following sections, we introduce a robust topological network criterion for quantitatively and qualitatively classifying quasi-one-dimensional and two-dimensional ice structures, specifically adapted for confined systems. We demonstrate the generality of our method by using it to identify structures of well-known one-dimensional nanoribbons and two-dimensional monolayer ices. We have also formulated a prism identification scheme for identifying the constituent building blocks of  $n$ -gonal one-dimensional ice. Our graph-theoretic network criterion leads to intuitive metrics for quantifying network structures, including the projected area, the occupied volume, and other similar topological features, which shed light on simulation results. We prove the efficacy of such analysis techniques for systems in higher temperature phases and transitions of monolayer ice within a graphite nanochannel. We show how our topological network parameter may be used for exploratory studies of entirely

new systems. Our order parameter as described is based on purely topological features, and makes no assumptions of the regularity of the local environment or symmetry factors, instead relying solely on the description of the hydrogen bonds.

## 2 Theory and methods

### 2.1 Topological network criterion

Visual inspection of confined systems (Fig. 1(a)) gravitates towards the identification of polygons. To this end, we have shown that the composition of the HBN in terms of  $n$ -membered rings may be used for classification purposes. Our definition of a ring is similar to that in the literature.<sup>24,28</sup> We define a ring as the largest polygon that can be formed from oxygen atoms of hydrogen-bonded molecules, such that it cannot be broken into smaller constituent rings. This is, in essence, the mathematical description of a primitive ring, using King's shortest path criterion.<sup>34</sup>

Here, we outline the methodology by applying it to fMSI (flat Monolayer Square Ice) formed within a graphene nanochannel.<sup>18</sup> In previous treatments of bulk ice and supercooled water, primitive ring analyses have been implemented using a fixed-distance cutoff.<sup>24,28</sup> However, we demonstrate that naive application of primitive ring analysis using a fixed-distance cutoff

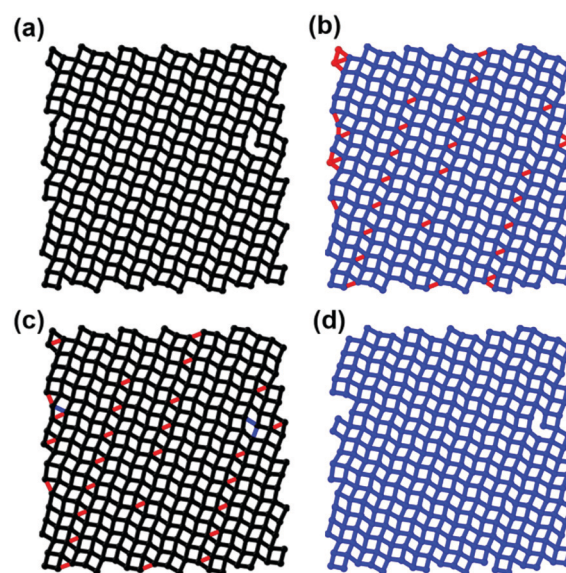


Fig. 1 Intermediate stages of our topological network criterion, in the classification of fMSI. (a) Top view of the hydrogen bonding network, determined using a strict geometric criterion. Only oxygen atoms have been shown. Molecules which participate in hydrogen bonds are connected by black bonds as shown. (b) 4-Membered rings (blue) and 3-membered rings (red), using a fixed-distance cutoff of 3.5 Å. Shared edges have been shown in blue. The ring network shown here has been created using primitive rings with a fixed-distance cutoff only. Several extra bonds are introduced. (c) HBN (black) overlaid over 4-membered rings (blue) and 3-membered rings (red). Extraneous bonds in blue and red are clearly visible. The extra triangular phase (red) is particularly prominent, which has no overlap with the HBN. (d) 4-Membered rings (blue) and 3-membered rings (red) after the application of our topological network criterion, eliminating superfluous bonds. No triangular phase remains.

introduces severe error, necessitating modifications of the methodology for confined systems. The ring network formed using a fixed-distance cutoff has been depicted in Fig. 1(b). Fig. 1(c) shows extraneous bonds, coloured in red and blue, caused by using primitive rings without accounting for the HBN, shown here in black. This visual representation shows how the HBN does not coincide with the ring network formed using a fixed-distance cutoff.

Our topological network criterion incorporates the information of the HBN, thus eliminating superfluous bonds with high accuracy. Fig. 1 depicts the various intermediate stages in the classification of fMSI formed within the graphene nano-capillary. Our methodology is as follows.

First, all molecules connected by hydrogen bonds are identified using a strict geometric criterion. Fig. 1(a) shows the HBN for fMSI, with connections between oxygen molecules which are hydrogen-bonded. In this particular treatment, no differentiation is made between donor and acceptor molecules. We define an oxygen atom to be hydrogen-bonded to a hydrogen atom if the angle between the O–O and O–H vectors is less than 30 degrees, and if the distance between the possible donor oxygen and acceptor hydrogen is less than 2.42 Å.<sup>35</sup>

Following this, we determine all possible primitive rings, from  $n = 3$  to  $n = 10$ . In this case, the number of primitive rings for  $n > 4$  is negligible. A distance cutoff of 3.5 Å is used, sufficient to encompass all first-neighbour shell molecules. However, there are still several extraneous bonds, clearly visible in Fig. 1(c).

Next, we eliminate all primitive rings with connections between molecules which are not hydrogen-bonded, using the previously determined HBN information. By eliminating such non-hydrogen bonded rings, we obtain precise connectivity information while still closely approximating the HBN.

On eliminating extra bonds, the resultant ring network in Fig. 1(d) almost perfectly coincides with the HBN in Fig. 1(a). Our topological criterion correctly classifies the monolayer ice as being primarily square ice, and entirely eliminates the superfluous triangular phase.

We have also tested our criterion by comparing its performance with that of Voronoi tessellation for the same fMSI phase described above, visually represented in Fig. 2. The accuracy of any identification scheme can be assessed by judging the extent to which it reproduces the connectivity of the HBN. Even after applying face area and edge length thresholds, Voronoi tessellation creates several extra connections (Fig. 2(c)). A perfectly accurate Voronoi diagram for this system would have had particles at the center of tetragonal Voronoi cells, corresponding to a coordination number of 4 for each particle. In fact, the bond network generated by Voronoi tessellation in Fig. 2(c) closely resembles the primitive ring network of Fig. 1(b), for whose generation the hydrogen bonds were not considered and only a fixed-distance cutoff was used.

The advantage of our topological network criterion for structural determination is its unambiguous classification of the hydrogen-bonded ring network in terms of  $n$ -membered primitive rings, even at ambient temperatures or under strong confinement.

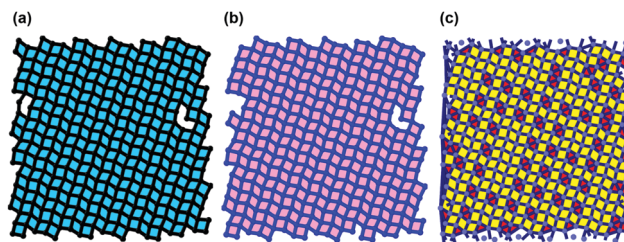


Fig. 2 Comparison of the accuracy of Voronoi tessellation with our topological network criterion for identifying fMSI. fMSI is known to consist of 4-membered polygons. (a) The top view of the HBN, with 4-membered polygons shaded in cyan. Identification schemes should closely approximate the HBN connectivity. (b) The ring network generated by our topological network criterion, with 4-membered rings shaded in pink. (c) Neighbour bonds created by Voronoi tessellation. The bonds (in black) are generated by connecting neighbouring particles (blue) which share a Voronoi face. Polygons thus formed, with three and four edges, are coloured in red and yellow, respectively. The Voronoi cells are 5-membered and 4-membered polygons, depending on the coordination number.

It is also clearly evident that, under such conditions, direct application of a primitive ring analysis using a fixed-distance cutoff introduces significant error. We observe that there is especially an increase in the erroneous identification of the triangular phase. Thus, keeping the non-hydrogen bonded extra connections (shown in Fig. 1(b)) causes the incorrect identification of ice. We also note that the extra connections do not satisfy the Bernal–Fowler ice rules.<sup>36</sup> fMSI, which is known to satisfy the ice-rules, visually indicates that the excess connections are not concurrent with the ice rules, while the reduced ring network in Fig. 1(d) does not, at least, appear to violate the ice rules.

However, one caveat of eliminating rings is that, for example, one or two 3-membered primitive rings may be removed, whose sides could have formed a 4-membered ring which was not previously not considered to be primitive according to the fixed-distance criterion. Such rings form a negligible percentage of the whole, and are in the vicinity of point defects or the edges. In this specific case, three sets of pairs of triangles on the left edge and right edge were removed (visible when comparing Fig. 1(b) and (d)). These actually form three 4-membered rings, which were also removed along with the extra bonds.

Depending on the number of nodes (three or four) in each ring, we note that the resulting topological network coincides with 98–100% of the HBN.

The ring network obtained from our topological network criterion may be used as-is for monolayer ice identification. Using these hydrogen-bonded rings as a basis, we develop a prism identification algorithm for identifying  $n$ -gonal prism blocks.

## 2.2 Prism identification algorithm

The structural building block of an  $n$ -sided prism is an assortment of two basal  $n$ -sided polygon planes, attached to each other by 4-membered lateral rings, as shown in Fig. 3. First, hydrogen-bonded  $n$ -membered rings are obtained according to the

procedure outlined above in Section 2.1. These are subsequently used to identify  $n$ -sided prism blocks.

We use the following recipe for identifying  $n$ -sided prisms. A pair of potential basal faces  $R_0 = m_1, m_2, \dots, m_n$  and  $R_1 = l_1, l_2, \dots, l_n$  is considered at a time. The 4-membered lateral faces connecting each pair of basal planes in a prism unit may be described solely by hydrogen bonds and do not need to be considered separately. The methodology is the same for any integral value of  $n > 2$ . Two candidate  $n$ -membered rings  $R_0$  and  $R_1$  are basal faces if the following conditions are true.

1.  $R_0 \cap R_1 = \emptyset$ .  $R_0$  and  $R_1$  should share no common nodes. They are only connected by hydrogen bonds.

2. Every node  $m_k$  in  $R_0$  must be a nearest neighbour of a corresponding node  $l_j$  in  $R_1$ , such that every node in  $R_0$  is hydrogen-bonded to exactly one node in  $R_1$ . For example, a node  $l_j$  in  $R_1$  cannot be connected to both  $m_k$  and  $m_{k+1}$  in  $R_0$ .

We apply our prism identification methodology to a zigzag (13,0) SWNT (single-walled nanotube), with  $R = 13$  corresponding to a diameter of 10.1 Å. The structure of the ice nanoribbon at 280 K, with a water occupancy of 1.23 g cm<sup>-3</sup>, is shown in Fig. 4. At this temperature, the nanoribbon is mostly comprised of tetragonal prisms, one triangular prism, and unclassified polygons in the middle. The rings which were classified as belonging to no  $n$ -sided prisms (unclassified) may denote the water phase, deformed prisms or a helical structure.

Specifically, the grey polygons in the top right inset of Fig. 4 are deformed tetragonal prisms. We note also that the relatively

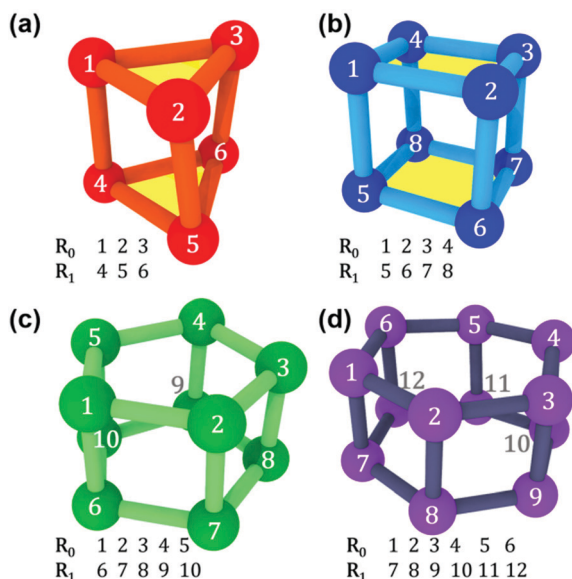


Fig. 3 Topology of the building blocks of (a) triangular, (b) tetragonal, (c) pentagonal and (d) hexagonal prisms. The identification algorithm is the same for any  $n$ -sided prism. The basal faces of the prisms have been shaded in yellow for the triangular and tetragonal blocks.  $R_0$  and  $R_1$  are the basal planes of the prism. The basal planes have no nodes in common. Each node  $m_k$ ,  $k \in [1, n]$ , in  $R_0$  is hydrogen-bonded to a corresponding node  $l_j$ ,  $j \in [1, n]$ , in  $R_1$ , where  $k$  and  $j$  are integral indices. Every  $m_k$  is only hydrogen-bonded to a single node  $l_j$ . In the case of tetragonal prisms, the basal faces and lateral faces are equivalent, but this does not affect the process of identification.

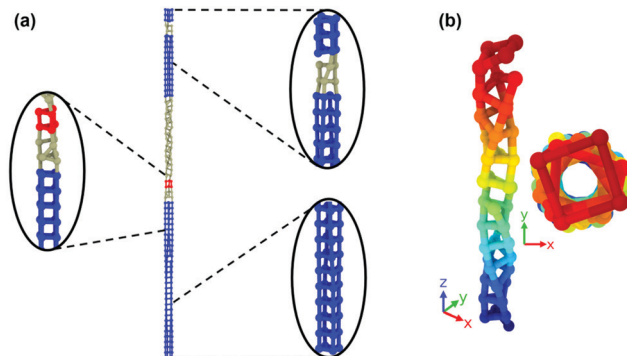


Fig. 4 Structures formed within a zigzag (13,0) SWNT, with explicit carbon atoms, at 280 K. (a) The full transverse view of the nanoribbon, post-classification of prismatic building blocks. The insets show close-up perspective views of sections of the nanoribbon. The tetragonal prisms, triangular prism and unclassified rings are coloured in blue, red and grey, respectively. The unclassified rings can denote either deformed prisms, helical order, or water molecules. The unclassified atoms in the upper right inset comprise a defective tetragonal prism. (b) Close-up perspective visual and top view of the unclassified atoms in the middle of the nanoribbon. They form a hollow helical structure exclusively composed of 4-membered rings. The atoms are coloured according to their heights.

twisted middle grey section of the nanoribbon has a hollow tube section, which indicates that it may be an ordered phase. It is also exclusively comprised of 4-membered polygons, coiled in a helical structure. The methodology for handling unknown nanoribbons with disparate structure compositions is given by the algorithm listed below:

1. First, obtain the hydrogen-bonded  $n$ -sided primitive rings for the system, such that ( $n > 2$ ).
2. Apply the prism determination algorithm for every  $n$ .
3. The unclassified structures remaining may be water, deformed prisms, or part of an ordered ladder-like or helical structure. Liquid water tends to form disordered rings of widely varying  $n$ , filling up the interior of the SWNT.<sup>4,37</sup> If the unclassified structure does not fill the interior of the nanotube and exhibits a certain degree of order, it may be part of a helical structure, or a deformed prism, depending on the symmetry. A simple indication of order is the number and type of primitive rings comprising the unclassified sections. In the case of the nanoribbon in Fig. 4, every unclassified molecule almost exclusively participates in only 4-membered rings. We also show, in subsequent sections, that our algorithm may be used to qualitatively describe the abrupt symmetry change in freezing icy nanoribbons.

### 2.3 Coverage area metric

The number of rings has been used as a qualitative metric in previous studies.<sup>23,24,26</sup> However, in our systems, 3-membered rings in the HBN are smaller in size than 4-membered rings, making the number of rings an unreliable descriptor (Fig. 5).

Intuitively, the area of each ring is a more qualitative metric for monolayer systems. In our monolayer simulation systems, water layers are formed in the  $XY$  plane. We define the  $XY$ -plane coverage area to be the projected area of each ring onto the  $XY$  plane. We normalize the coverage area by the theoretical maximum

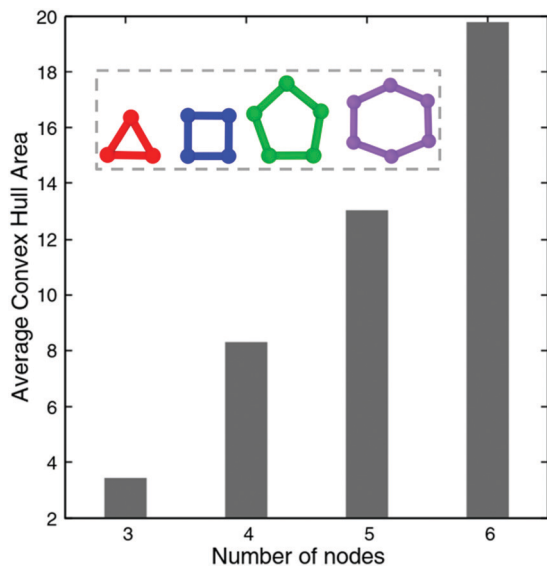


Fig. 5 Average convex hull areas of  $n$ -membered rings observed in our systems. The convex hulls<sup>38</sup> are formed from the vertices of the  $n$ -membered rings. 4-Membered rings are approximately more than double the size of 3-membered rings, a conclusion which is supported by visual inspection of the HBN of fMSI within graphene nano-confinement. The insets show top views of typical  $n$ -membered rings observed in monolayer and nanoribbon ices.

possible area of the ice, which, in the case of monolayer water, is the area of the confining sheet. The coverage area percentage is the percentage of the total area of the constraining sheet that is comprised of the projected area of  $n$ -membered rings, where  $n > 2$

$$\text{Coverage area percentage}_n = \frac{\sum_{i=1}^{i=N_n} A_i}{\text{Area of sheet}} \times 100$$

where  $A_i$  is the projected area of the  $i$ th  $n$ -membered ring, and  $N_n$  is the total number of  $n$ -membered rings.

The coverage area metric does not distinguish between small isolated clusters of  $n$ -membered rings, and a contiguous connected cluster. It is possible to apply additional constraints for connected rings of certain types to identify ices like fMSI and pMSI (puckered Monolayer Square Ice), which are composed of a single type of ring. We have observed that thermal fluctuations momentarily fracture the ring network, which could disrupt the connectivity of large swathes of ordered rings. For the monolayer ices studied in this work, the coverage area percentage was found to describe phase transitions and relative proportions of  $n$ -membered rings accurately.

#### 2.4 Occupied volume metric

We formulate a qualitative volume-based metric to determine the relative proportions of  $n$ -gonal prism structures within nanoribbons. Our prism determination algorithm produces pairs of  $n$ -sided basal rings. We obtain the volume enclosed by the prism block by calculating the volume of the convex hull<sup>38</sup> formed by the basal ring vertices. For  $n \neq 4$ , the basal

rings are perpendicular to the axis, but for  $n = 4$ , we only consider axial rings to prevent overcounting.

For every  $n$ , the total volume of each  $n$ -gonal prismatic phase is obtained by summing over the convex hull volumes of the prism blocks. We normalize this volume by the maximum possible volume, which is the occupied volume if an  $n$ -sided prism were to fill the entire cylinder height. The maximum possible length of each edge is 3.5 Å from solvation shell considerations. We have observed that the volume of each prism block for a particular  $n$  is relatively constant, thermal fluctuations notwithstanding. Thus, for a particular prism phase, whose basal face has  $n$  nodes, we can approximate the maximum possible filled volume by assuming that the SWNT is filled by a regular  $n$ -gonal prism of height  $h$ :

Maximum possible volume <sub>$n$</sub>  = Convex hull area of basal ring  $\times h$

where  $h$  is the length of the SWNT.

Thus, we define the occupied volume percentage for an  $n$ -gonal prismatic phase as:

$$\text{Occupied volume percentage}_n = \frac{\sum_{i=1}^{i=N_n} V_i}{\text{Maximum possible volume}_n} \times 100$$

where  $V_i$  the convex hull volume of the  $i$ th  $n$ -gonal prism block, and  $N_n$  is the total number of  $n$ -gonal prism blocks.

The maximum possible volume which we have used as a normalizing factor varies for a particular  $n$ . This is because the effective area of the basal ring is different for every  $n$ , with trigonal basal rings occupying the least area. A consequence of this is that the sum of the occupied volume of various composite  $n$ -gonal blocks is always less than the total volume. We prove in subsequent sections that this occupied volume percentage is an accurate qualitative measure of phase transitions.

### 3 Simulation details

We have studied the following systems: (1) monolayer ice systems with explicit carbon atoms for simulating rigid graphene layers, and nanoribbon ices constrained by single-walled nanotubes (2) with smooth featureless walls, and (3) with explicit carbon atoms. The systems simulated are well-known in the literature and have thus been used for validation and benchmarking.

For the monolayer ice graphene water system, the simulation setup is similar to systems reported in the literature,<sup>18</sup> shown in Fig. 6. A nanochannel was created by introducing a gap width  $h$  between a pair of three graphene sheets. Two water reservoirs, containing 2000 molecules, were placed on either side of the nanochannel thus formed. The dimensions of the sheets were 50.349 Å  $\times$  50.349 Å in the  $X$  and  $Y$  dimensions, respectively. We used center-to-center separation widths between the parallel graphene sheets of 6 Å, which is sufficient to permit the formation of a single layer of water.

We have used LAMMPS<sup>39</sup> to run equilibrium Molecular Dynamics simulations. Lateral pressures were applied in the  $X$  dimension. The MD simulations were performed in the

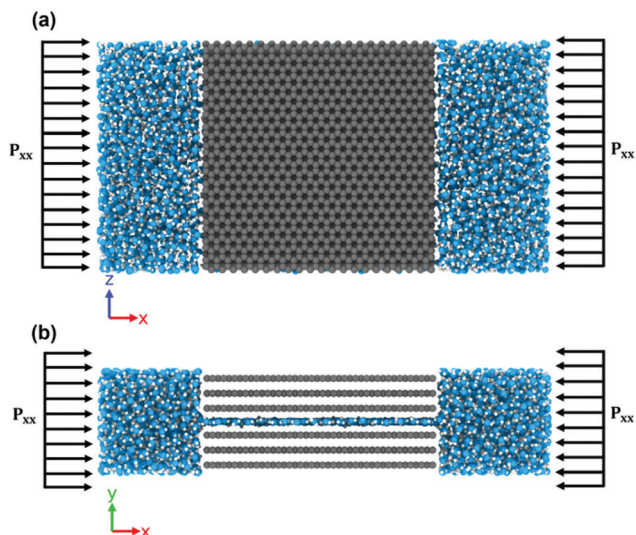


Fig. 6 Representative views of the water monolayer constrained by graphene sheets. The graphene atoms are indicated in dark-grey; the oxygen atoms are light blue and the hydrogen atoms are white. (a) Top view of the simulation system, showing the XY plane. (b) Side view of the simulation system, showing the XZ plane. The center-to-center separation width between the parallel graphene layers is the gap separation width,  $h$ .

isothermal–isobaric ( $NP_{xx}T$ ) ensemble. The temperature ( $T$ ) and pressure ( $P_{xx}$ ) were controlled by the Nose–Hoover thermostat and barostat, respectively. A timestep of 1 fs was used for the velocity-Verlet integration scheme. The particle–particle–particle mesh (PPPM) algorithm was used for computing the long-range interactions.

TIP4P/2005<sup>40</sup> was used to model the water molecules in all the systems studied in this work. Among the commonly used rigid water models used for simulating confined systems, TIP4P/2005 performs reliably well compared to other popular rigid water models.<sup>21</sup> The sum of the interactions between the TIP4P/2005 molecules, and the external Lennard-Jones potential of interaction between the water molecules and the confining sheet yields the total potential of interaction.

In this work, we have used Lennard-Jones force-field parameters for the interactions between the oxygen atoms of water and the carbon atoms of graphene.<sup>41</sup> These parameters have been extensively used for graphite and water, accurately reproducing the contact angle of water on graphite.<sup>10,11,18,20</sup>

For the SWCNT simulations, the methodology of previous literature was used,<sup>1,4</sup> and the featureless walls were simulated using the 9-3 Lennard-Jones potential.<sup>42,43</sup> The explicit carbon atoms were modeled using the OPLS force field.<sup>44</sup>

The visuals in this work were created using OVITO.<sup>45</sup> Primitive rings were obtained using R.I.N.G.S.<sup>46</sup> These rings were further analysed according to our topological network criterion.

## 4 Results and discussion

### 4.1 Freezing of an ice nanotube

We investigate the phase changes of water confined within a (13,0) featureless SWCNT, corresponding to a diameter of 10.1 Å.

The system was equilibrated at 320 K for 20 ns at a pressure of 0.1 MPa, following which the temperature was lowered in steps of 10 K. At each temperature, the simulations were performed for 20 ns at a pressure of 1 MPa. When the temperature is lowered in this manner from 320 K, at a constant axial pressure of 1 MPa, an abrupt change in state from the liquid phase is observed at 270 K. The occupied volume percentage rises suddenly from 0% to  $\approx 53\%$  and  $\approx 17\%$  for the pentagonal and hexagonal blocks, respectively (Fig. 7(b)). No other  $n$ -gonal prism structures are present. A supplementary movie (liqToSolidINT.avi in the ESI†) depicts this phase transition from the liquid phase at 270 K.

The prism determination criterion is also able to capture solid-to-solid phase transitions. Fig. 7(a) shows the quasi-one-dimensional water in four states: liquid water at 290 K; System A at 270 K after a simulation time of 240 ps, following the abrupt change in state from liquid to solid; System B after 20 ns at 270 K; and System C at 240 K. Initially, at 270 K (System A in Fig. 7(a)), a higher proportion of pentagonal prismatic ice is observed. However, we observe a gradual change of the pentagonal blocks to hexagonal blocks. After 20 ns simulation at 240 K the nanoribbon becomes almost exclusively comprised of hexagonal prism blocks (System C in Fig. 7(a)).

### 4.2 Monolayer within a graphene nanocapillary

Monolayer water exists in the form of fMSI when it is constrained between two graphene surfaces 6 Å apart at 1 GPa and 300 K.<sup>10</sup> fMSI exhibits a first-order phase transition when it is subjected to superheating at a constant low lateral pressure ( $P_{zz} = 1$  GPa).<sup>20</sup>

We have performed heating and cooling MD simulations of fMSI, using a simulation setup similar to those previously used in the literature.<sup>10,18,20</sup> Concomitant with the literature, we observe an abrupt increase in the potential energy per molecule

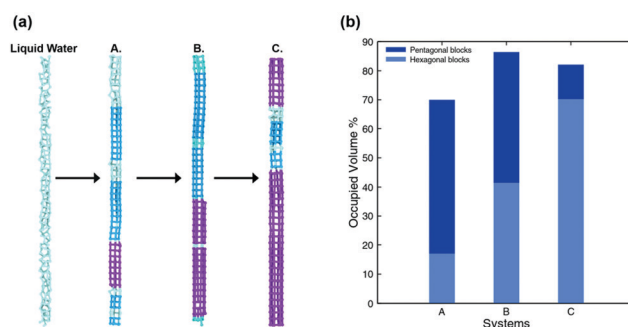
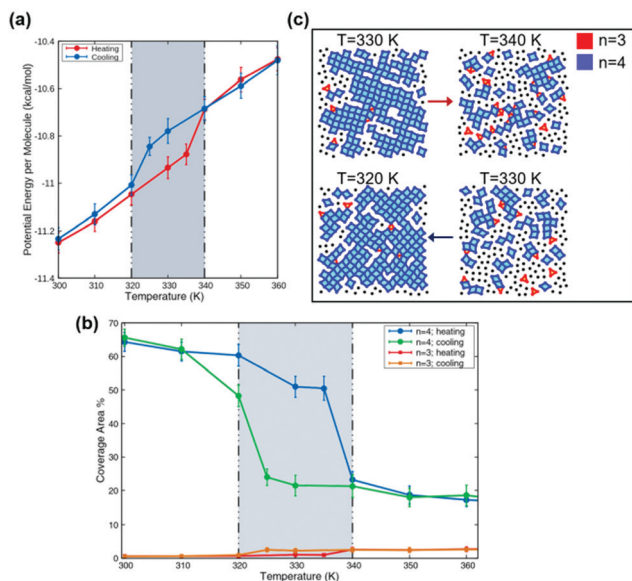


Fig. 7 Pentagonal and hexagonal prismatic ice evolution in a (13,0) featureless SWCNT. (a) Snapshots of the water nanoribbon, as the temperature is lowered from 290 K to 240 K. The particles and bonds are coloured in purple (hexagonal blocks), blue (pentagonal blocks) and light cyan (unclassified), as classified by our prism identification criterion. At 290 K, the nanoribbon is completely water. Systems A and B correspond to the nanoribbon at 270 K, just after abrupt freezing and after 20 ns respectively. System C shows the nanoribbon at 240 K. (b) Occupied volume percentage for the pentagonal and hexagonal blocks, showing the change in the relative proportions of the two ice types.



**Fig. 8** The first-order transitions observed in the heating and cooling of fMSI. (a) Potential energy per molecule change with temperature during the heating (solid red line) and cooling (solid blue line) process. (b) The coverage area percentage plotted against temperature, for 4-membered and 3-membered rings. Here  $n$  is the number of nodes in each type of ring. (c) Snapshots of the monolayer during the heating and cooling process, visually depicting the coverage area. The arrows are in the direction of increasing and decreasing temperature for the heating and cooling process respectively. 4-Membered rings (blue) and 3-membered rings (red) are shaded in cyan and orange, respectively. Particles which do not participate in the ring network are coloured in black.

of  $\approx 0.2 \text{ kcal mol}^{-1}$ , corresponding to the disruption of the ordered HBN (Fig. 8(a)).

The plot of the coverage area percentage for 4-membered rings in Fig. 8(b) shows a sharp decrease by  $\approx 25\%$  when the temperature is increased to 340 K during the heating process. The coverage area percentage of 3-membered rings also changes during this phase transition. The disordered liquid network tends to have a relatively higher proportion of 3-membered rings (visually discernible in Fig. 8(c)). However, fMSI has negligible proportions of 3-membered rings. When the monolayer is pMSI, the coverage area percentage of the 3-membered rings remains constant at  $\approx 0\%$ . The hysteresis loop of the 3-membered rings echoes that of the 4-membered rings and the potential energy per molecule.

pMSI has been reported to form in a graphene nano-channel with a slit width of  $7 \text{ \AA}$ , at 300 K and 2 GPa.<sup>10</sup> Fig. 9(a) shows the potential energy per molecule change during the heating and cooling of pMSI, at a constant lateral pressure of 2 GPa. The coverage area percentage hysteresis loops mirror the hysteresis loop in the potential energy per molecule. The trends suggest that the phase transition is a first-order transition. The coverage area percentage change for the 3-membered rings (Fig. 9(b)) is more significant for pMSI than for fMSI (Fig. 8(b)).

Thus, the coverage area percentage is able to reproduce trends in the potential energy per molecule, showing a correspondingly large hysteresis loop.

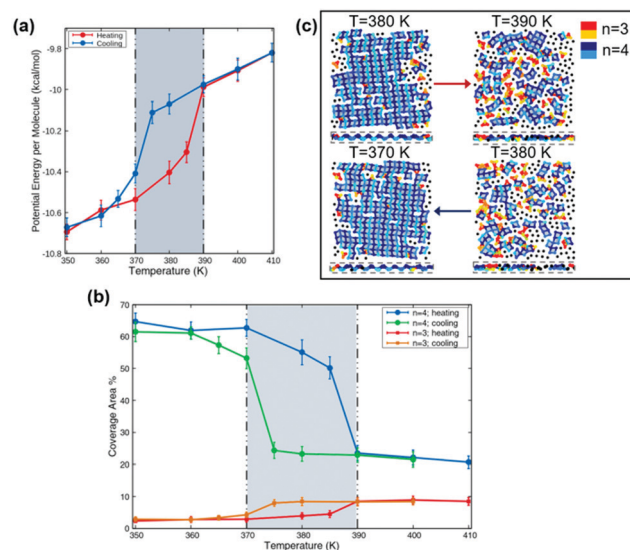


**Fig. 9** The phase transitions observed in the heating and cooling of pMSI at 2 GPa. (a) Potential energy per molecule plotted against the temperature during the heating and cooling process. (b) The coverage area percentage change with temperature, for 4-membered and 3-membered rings. (c) Snapshots of the puckered monolayer during the heating and cooling process, with the coverage area visually depicted by shaded-in  $n$ -membered rings. Arrows are in the directions of increasing and decreasing temperature for the heating and cooling process, respectively. The insets show the puckered nature of the monolayer. Particles of the 4-membered rings and 3-membered rings are coloured in shades of blue and orange-red, respectively, according to the height. 4-Membered and 3-membered rings are shaded in grey and orange, respectively. Particles outside the ring network are coloured in black.

## 5 Conclusions

In this work we have presented a general and extensible family of topological network criteria for the structural identification and analysis of quasi-one-dimensional and two-dimensional ices. The primitive rings, identified using a fixed-distance cutoff, are screened to obtain rings whose connections correspond to the HBN. Explicitly accounting for the hydrogen bonds in confined ordered structures has been found to be necessary. The effects of confinement may force molecules to be clustered within a fixed distance cutoff corresponding to the first nearest-neighbour shell, but they are additionally constrained by the viability of hydrogen bonds. We show how the reduction of non-hydrogen bonded connections is crucial to prevent mis-identification of fMSI. The primitive rings may be further analysed for further identification, or used as-is.

We use the primitive rings so obtained as a basis for an algorithm for identifying the building blocks of  $n$ -sided prisms. Our prism identification algorithm classifies the  $n$ -membered prism blocks which comprise single ice nanotubes (INTs). Helical structures and deformed prisms are not identified by this particular recipe, but can still be distinguished from the liquid state by virtue of the number and type of the component primitive rings. We show how a modified projected area, the coverage area metric, may be used as an order parameter for investigating the phase transitions in monolayer water. The

coverage area percentage for every  $n$  is a measure of the relative proportion of the  $n$ -membered rings. We have also developed an analogous volume-based order parameter for INT classification. In the same spirit as that of the coverage area metric, we reinterpret the topological features from a molecular simulation analysis perspective. The occupied volume percentage is calculated using the convex hull volumes of component prism blocks identified using the prism determination recipe. Both these metrics are able to qualitatively describe various pressure-induced and temperature-induced phase transitions.

The topological network criterion that forms the basis of these related methodologies is flexible and easily customizable, requiring no *a priori* assumptions beyond those for hydrogen bonds. We envisage that other interconnected networks, including multi-component structures and solid-liquid interfaces, may be probed using this general approach. The relative speed of the criterion presented here and the scope for parallelization make it possible to consider using it for on-the-fly calculations during simulation runs, at least for small systems.

We anticipate that these sets of techniques may have wider applicability for other confined structures and geometries, especially those with mixed structures of unknown relative composition.

## Conflicts of interest

There are no conflicts to declare.

## Acknowledgements

This work was supported by the Department of Science and Technology, Govt of India. Computational resources were provided by the HPC cluster of the Computer Center (CC), Indian Institute of Technology Kanpur.

## Notes and references

- 1 K. Koga, G. T. Gao, H. Tanaka and X. C. Zeng, *Nature*, 2001, **412**, 802–805.
- 2 A. Kalra, S. Garde and G. Hummer, *Proc. Natl. Acad. Sci. U. S. A.*, 2003, **100**, 10175–10180.
- 3 J. H. Walther, K. Ritos, E. R. Cruz-Chu, C. M. Megaridis and P. Koumoutsakos, *Nano Lett.*, 2013, **13**, 1910–1914.
- 4 D. Takaiwa, I. Hatano, K. Koga and H. Tanaka, *Proc. Natl. Acad. Sci. U. S. A.*, 2007, **105**, 39–43.
- 5 W.-H. Zhao, J. Bai, L.-F. Yuan, J. Yang and X. C. Zeng, *Chem. Sci.*, 2014, **5**, 1757–1764.
- 6 J. Bai, C. A. Angell and X. C. Zeng, *Proc. Natl. Acad. Sci. U. S. A.*, 2010, **107**, 5718–5722.
- 7 G. Algara-Siller, O. Lehtinen, F. C. Wang, R. R. Nair, U. Kaiser, H. A. Wu, A. K. Geim and I. V. Grigorieva, *Nature*, 2015, **519**, 443–445.
- 8 K. V. Agrawal, S. Shimizu, L. W. Drahushuk, D. Kilcoyne and M. S. Strano, *Nat. Nanotechnol.*, 2016, **12**, 267–273.
- 9 K. Mochizuki and K. Koga, *Proc. Natl. Acad. Sci. U. S. A.*, 2015, **112**, 8221–8226.
- 10 Y. Zhu, F. Wang, J. Bai, X. C. Zeng and H. Wu, *ACS Nano*, 2015, **9**, 12197–12204.
- 11 Y. Zhu, F. Wang, J. Bai, X. C. Zeng and H. Wu, *J. Phys. Chem. C*, 2016, **120**, 8109–8115.
- 12 P. Hirunsit and P. B. Balbuena, *J. Phys. Chem. C*, 2007, **111**, 1709–1715.
- 13 H. Mosaddeghi, S. Alavi, M. H. Kowsari and B. Najafi, *J. Chem. Phys.*, 2012, **137**, 184703.
- 14 J. J. Gilvarry, *Phys. Rev. Lett.*, 1966, **16**, 1089–1091.
- 15 X. H. Zheng and J. C. Earnshaw, *Europhys. Lett.*, 1998, **41**, 635–640.
- 16 C. K. Das and J. K. Singh, *Theor. Chem. Acc.*, 2013, **132**, 1351.
- 17 W.-H. Zhao, L. Wang, J. Bai, L.-F. Yuan, J. Yang and X. C. Zeng, *Acc. Chem. Res.*, 2014, **47**, 2505–2513.
- 18 L. Yang, Y. Guo and D. Diao, *Phys. Chem. Chem. Phys.*, 2017, **19**, 14048–14054.
- 19 J. Chen, G. Schusteritsch, C. J. Pickard, C. G. Salzmann and A. Michaelides, *Phys. Rev. Lett.*, 2016, **116**, 025501.
- 20 Y. Zhu, F. Wang and H. Wu, *J. Chem. Phys.*, 2017, **146**, 134703.
- 21 J. Dix, L. Lue and P. Carbone, *J. Comput. Chem.*, 2018, **39**, 2051–2059.
- 22 X. Yuan and A. Cormack, *J. Non-Cryst. Solids*, 2001, **283**, 69–87.
- 23 V. Chihaiia, S. Adams and W. F. Kuhs, *Chem. Phys.*, 2005, **317**, 208–225.
- 24 C. G. Salzmann, P. G. Radaelli, B. Slater and J. L. Finney, *Phys. Chem. Chem. Phys.*, 2011, **13**, 18468.
- 25 K. Goetzke and H.-J. Klein, *J. Non-Cryst. Solids*, 1991, **127**, 215–220.
- 26 Z. Zhang and G.-J. Guo, *Phys. Chem. Chem. Phys.*, 2017, **19**, 19496–19505.
- 27 Prerna, R. Goswami, A. K. Metya, S. V. Shevkunov and J. K. Singh, *Mol. Phys.*, 2019, 1–13.
- 28 A. Haji-Akbari and P. G. Debenedetti, *Proc. Natl. Acad. Sci. U. S. A.*, 2015, **112**, 10582–10588.
- 29 G. C. Sosso, T. Li, D. Donadio, G. A. Tribello and A. Michaelides, *J. Phys. Chem. Lett.*, 2016, **7**, 2350–2355.
- 30 S. Saito, B. Bagchi and I. Ohmine, *J. Chem. Phys.*, 2018, **149**, 124504.
- 31 G. C. Sosso, J. Chen, S. J. Cox, M. Fitzner, P. Pedevilla, A. Zen and A. Michaelides, *Chem. Rev.*, 2016, **116**, 7078–7116.
- 32 F. Sciortino and S. L. Fornili, *J. Chem. Phys.*, 1989, **90**, 2786–2792.
- 33 P. Pugliese, M. M. Conde, M. Rovere and P. Gallo, *J. Phys. Chem. B*, 2017, **121**, 10371–10381.
- 34 S. V. King, *Nature*, 1967, **213**, 1112–1113.
- 35 A. Chandra, *J. Phys. Chem. B*, 2003, **107**, 3899–3906.
- 36 J. D. Bernal and R. H. Fowler, *J. Chem. Phys.*, 1933, **1**, 515–548.
- 37 M. Raju, A. van Duin and M. Ihme, *Sci. Rep.*, 2018, **8**, 1836–1842.
- 38 C. B. Barber, D. P. Dobkin and H. Huhdanpaa, *ACM Trans. Math. Software*, 1996, **22**, 469–483.
- 39 S. Plimpton, *J. Comput. Phys.*, 1995, **117**, 1–19.

- 40 J. L. F. Abascal and C. Vega, *J. Chem. Phys.*, 2005, **123**, 234505.
- 41 T. Werder, J. H. Walther, R. L. Jaffe, T. Halicioglu and P. Koumoutsakos, *J. Phys. Chem. B*, 2003, **107**, 1345–1352.
- 42 P. Kumar, S. V. Buldyrev, F. W. Starr, N. Giovambattista and H. E. Stanley, *Phys. Rev. E: Stat., Nonlinear, Soft Matter Phys.*, 2005, **72**, 051503.
- 43 S. Han, M. Y. Choi, P. Kumar and H. E. Stanley, *Nat. Phys.*, 2010, **6**, 685–689.
- 44 W. L. Jorgensen, D. S. Maxwell and J. Tirado-Rives, *J. Am. Chem. Soc.*, 1996, **118**, 11225–11236.
- 45 A. Stukowski, *Modell. Simul. Mater. Sci. Eng.*, 2009, **18**, 015012.
- 46 S. L. Roux and P. Jund, *Comput. Mater. Sci.*, 2010, **49**, 70–83.